Conference paper

Aleksandar Živković, Jacobina Sheehama, Michael E. A. Warwick, Daniel R. Jones, Claire Mitchel, Daniel Likius, Veikko Uahengo, Nelson Y. Dzade, Sankar Meenakshisundaram, Charles W. Dunnill* and Nora H. de Leeuw*

Structural and electronic properties of Cu_4O_3 (paramelaconite): the role of native impurities

https://doi.org/10.1515/pac-2021-0114

Abstract: Hybrid density functional theory has been used to study the phase stability and formation of native point defects in Cu_4O_3. This intermediate copper oxide compound, also known as paramelaconite, was observed to be difficult to synthesize due to stabilization issues between mixed-valence Cu^{1+} and Cu^{2+} ions. The stability range of Cu_4O_3 was investigated and shown to be realized in an extremely narrow region of phase space, with Cu_2O and CuO forming readily as competing impurity phases. The origin of *p*-type conductivity is confirmed to arise from specific intrinsic copper vacancies occurring on the 1+ site. Away from the outlined stability region, the dominant charge carriers become oxygen interstitials, impairing the conductivity by creating deep acceptor states in the electronic band gap region and driving the formation of alternative phases. This study further demonstrates the inadequacy of native defects as a source of *n*-type conductivity and complements existing experimental findings.

Keywords: Chemistry and its applications; Cu_4O_3; density functional theory (DFT); instrinsic defects; paramelaconite; p-type conductivity; VCCA-2020.

Introduction

Paramelaconite (Cu_4O_3) is the least explored oxide of copper. First reports on the structure of Cu_4O_3 date back to the works of Clifford Frondel [1] and Datta et al. [2], who defined paramelaconite as an oxygen-deficient tetragonal copper oxide, where the omission of oxygen atoms is compensated by the appearance of cuprous

Article note: A collection of invited papers based on presentations at the Virtual Conference on Chemistry and its Applications (VCCA-2020) held on-line, 1–31 August 2020.

***Corresponding authors: Charles W. Dunnill**, Energy Safety Research Institute, Swansea University, Bay Campus, Fabian Way, Swansea SA1 8EN, UK; and **Nora H. de Leeuw**, School of Chemistry, Cardiff University, Main Building Park Place, Cardiff CF10 3AT, UK; Department of Earth Sciences, Utrecht University, Princetonlaan 8a, 3548CB Utrecht, The Netherlands; and School of Chemistry, University of Leeds, Woodhouse Lane, Leeds LS2 9JT, UK, e-mail: C.Dunnill@swansea.ac.uk (C. W. Dunnill), N.H.deLeeuw@leeds.ac.uk (N. H. de Leeuw).
Aleksandar Živković, School of Chemistry, Cardiff University, Main Building Park Place, Cardiff CF10 3AT, UK; and Department of Earth Sciences, Utrecht University, Princetonlaan 8a, 3548CB Utrecht, The Netherlands
Jacobina Sheehama, Daniel Likius and Veikko Uahengo, Department of Chemistry and Biochemistry, University of Namibia, 340 Mandume Ndemufayo Avenue, Windhoek 9000, Namibia
Michael E. A. Warwick and Daniel R. Jones, Energy Safety Research Institute, Swansea University, Bay Campus, Fabian Way, Swansea SA1 8EN, UK
Claire Mitchel, Nelson Y. Dzade and Sankar Meenakshisundaram, School of Chemistry, Cardiff University, Main Building Park Place, Cardiff CF10 3AT, UK

ions in place of cupric ones. However, both proposed structures had a unit cell content of $Cu_{16}O_{14}$, which was later attributed to the presence of admixed CuO in the sample. A refined structure with the unit cell content of $Cu_{16}O_{12}$ (*i.e.*, Cu_4O_3) was identified by O'Keeffe and Bovin [3]. The correct chemical formula of paramelaconite is $Cu_2^{1+}Cu_2^{2+}O_3$, with two distinct copper atoms, Cu(1) and Cu(2). The first one, Cu(1), is cuprous copper and has two nearest neighbour oxygen atoms, O(1), forming collinear bonds of length 1.87 Å as found in Cu_2O. In contrast, Cu(2) is cupric copper and is surrounded by four oxygen atoms in an almost square planar configuration with bond lengths varying between 1.92 and 1.97 Å. Paramelaconite was indexed with a tetragonal cell with lattice parameters reading $a = b = 5.837$ and $c = 9.932$ Å (space group $I4_1/amd$, Number 141). The non-equivalent atomic positions are listed in Table 1.

Structural stability

The structure of Cu_4O_3 can be thought of as derived from CuO by ordered removal of oxygen atoms or derived from Cu_2O by ordered insertion of oxygen atoms – an intermediate stoichiometry between cupric and cuprous oxide. The name paramelaconite itself was derived from an old term used to describe the mineral CuO, namely melaconite [4]. Due to its unique stoichiometry, it is very difficult to synthesize Cu_4O_3 and particularly stabilize the mixed Cu^{1+} and Cu^{2+} valence ions [5]. The first experimental observation and successful synthesis of Cu_4O_3 dates back to the work of Long et al. [6]. They observed that the reduction of CuO to Cu using high resolution electron microscopy proceeded via at least two intermediate phases – Cu_4O_3 and Cu_2O. Paramelaconite was observed to be sensitive to air oxidation due to different valence copper atoms within the structure, hence the observed decomposition into Cu_2O and Cu at 350 °C and pure Cu at 500 °C. However, it was observed to be stable in air at 250 °C for 0.55 μm thick samples and 350 °C for 3.2 μm thick films [7]. In other words, the thickness and orientation of the films influence the stability and conversion temperature of Cu_4O_3 in air. In a separate study, Cu_4O_3 was observed to be stable up to 250 °C (520 K) when annealed in air [8]. It was also emphasized that upon annealing of Cu_4O_3 at 410 °C (683 K) a phase conversion into CuO is observed, as well as a further conversion into Cu_2O at 450 °C (723 K). Similarly, experiments conducted by Wang et al. [9] observed a decomposition of candy-like Cu_4O_3 micro-structures into CuO and Cu_2O at 400 °C (673 K). More recently, a copper-oxide based catalyst powder enriched with paramelaconite was found to be stable and perform well under industrially relevant current densities, forming ethylene as the main product [10]. Patwary et al. synthesized Cu_4O_3 films in an ambient of Ar and O_2 plasma using a pure Cu target and identified that oxygen partial pressures of 7.9–9.1 % were required to grow pure phase Cu_4O_3 [11].

Electronic properties

Based on UV-visible transmission measurements, a direct gap of 2.47 eV and an indirect band gap of 1.34 eV were measured [7] (see Table 2 for complete results). The measured absorption coefficient for Cu_4O_3 reaches a value of $1 \cdot 10^5$ cm^{-1} at a value of 2.4 eV. The rise of absorbance ($\lambda \leq 500$ nm) was derived from the direct band gap of 2.25 eV, while the light absorption corresponding to the indirect band gap (1.5 eV) was found to be relatively less effective [12].

Table 1: Wyckoff sites and fractional coordinates of non-equivalent atomic positions in Cu_4O_3 after O'Keeffe and Bovin [3].

Atom	Site symmetry	*x*	*y*	*z*
Cu^{1+}	8d	0.00000	0.00000	0.50000
Cu^{2+}	8c	0.00000	0.00000	0.00000
O–1	8e	0.00000	0.25000	0.61730
O–2	4a	0.00000	0.75000	0.12500

Table 2: Electronic properties of Cu_4O_3 found in existing literature.

Electronic band gap (indirect)	1.34 [7], 1.5 eV [19]
Electronic band gap (direct)	2.47 [7], 1.75 eV [20]
	2.3 eV [19]

Magnetic and transport properties

Paramelaconite was measured to order antiferromagnetically below 40 K with a propagation vector $\vec{k} = \left(\frac{1}{2}, \frac{1}{2}, \frac{1}{2}\right)$ with respect to the reciprocal basis of the conventional body centred cell [13]. The authors were unable to explain the observed magnetic ordering within models limited to isotropic super-exchange interactions, speculating upon the need to invoke higher order interactions or anisotropic exchange. Djurek et al. [14] observed an antiferromagnetic ordering of nanoscaled Cu_4O_3 at $T < 55$ K together with an additional transition at $T = 120$ K, whose ordering was not clarified. Hall effect measurements indicate that Cu_4O_3 is a *p*-type semiconductor [8]. The reported activation energy, in other words the thermal energy required for holes to jump into the valence band, is read as 0.14 eV, which lies around the reported values of CuO (0.12–0.16 eV) but below those of Cu_2O (0.20–0.24 eV). Thermo-power measurements confirmed the *p*-type conductivity of Cu_4O_3 samples with a single thermal hole activation energy (ionization energy of acceptors) of 0.12 eV [11]. Two high temperature conduction activation energies were measured at 0.29 and 0.41 eV (depending on oxygen flow rate synthesis conditions) and one low temperature conduction activation energy of ≈0.21 eV.

Theoretical investigations

Initial theoretical studies of Cu_4O_3 date back, to the best knowledge of the author, to a hybrid-DFT (B3LYP) study of Tejada-Rosales et al. [15]. Within their work, they investigated the structure and magnetic exchange interactions (between nearest neighbouring Cu atoms) and obtained values of $J_a = -11.1$ cm^{-1} (for the interaction along of Cu atoms along the chains) and $J_c = -9.8$ cm^{-1} (for the interaction between neighbouring perpendicular chains). More recently, DFT calculations using the L(S)DA+U approach were used to study the vibrational properties of both CuO and Cu_4O_3, obtaining good agreement with experimental values [16]. A clear distinction between CuO and Cu_4O_3 was observed based on the peak positions in the Raman spectrum, making it a useful probe for phase analysis.

Heinemann et al. [17] studied the structural stability and electronic structure of all three copper oxides using the LDA+U and hybrid (HSE06) functional calculations within DFT. The reported electronic energy gaps are in good agreement with experiment for Cu_2O, while CuO and Cu_4O_3 showed discrepancies between theory and experiment.

Debbichi et al. [18] studied the lattice dynamics for paramelaconite using the LDA+U approximation. From the calculated phonon band structures a dynamic stability was noted, as no soft modes were detected. Furthermore, the magnetic exchange coupling constants between neighbouring Cu^{2+} sites were calculated, yielding values of $J_1 = -18.2$ and $J_1 = -12.6$ meV, implying frustrated antiferromagnetism within Cu_4O_3. By including vibrational energy contributions to the total energy, the influence on the instability of Cu_4O_3 at elevated temperatures was illustrated.

Recently, Wang et al. [21] performed calculations within the *GW* method (highly accurate many-body perturbation technique) of the full optical absorption spectrum (both in the independent particle approximation and including excitonic effects) and quasi-particle densities of state for all three copper oxides. The *GW* calculations predict an indirect gap of 0.84 eV and a direct gap of 1.59 eV with an absorption onset of 1.61 eV in the IPA for Cu_4O_3. Excitonic effects were found to cause a redshift in the absorption spectrum of about 150 meV.

Despite the different subgap absorption mechanisms proposed, the prediction of an indirect band gap for Cu_4O_3 was confirmed through the experimentally and theoretically measured absorption spectrum.

Aim of current study

The majority of works concerning Cu_4O_3 treat the determination of its structural parameters and composition (experimentally), or electronic structure and absorption spectra (theoretically). However, little is known about defects present in Cu_4O_3, apart from its *p*-type conductivity, stemming from Hall measurement. The question of creating *n*-type Cu_4O_3 was neglected as well. The current work presents a joint experimental and theoretical study of the electronic ground state properties of Cu_4O_3. In addition, native impurities occurring in Cu_4O_3 are explored (using hybrid-DFT) together with the single-particle levels they eventually form in the pristine electronic band structure. An attempt is made to answer the following questions: (i) What is the role of simple impurities in the stability of Cu_4O_3? (ii) Can Cu_4O_3 be created intrinsically *n*-type? In order to do so, a comprehensive first-principles study of the geometry and electronic structure of Cu_4O_3 with induced defects was undertaken.

Experimental and computational details

Experiments

Materials

All reagents were of analytical grade and used without further purification. Distilled water was used in all experiments. The powders were synthesized using a solvothermal method adapted from Zhao et al. [5]. In a synthesis, N,N-dimethylformamide (DMF) and ethanol were mixed in a 1:2 vol ratio to form the reaction solvent. $Cu(NO_3)_2 \cdot 3H_2O$ was dissolved in 75.0 mL of this solvent to form a precursor solution of 0.07 M. The precursor solution was stirred for 15 min to form a clear solution. The reactions took place in a 150 mL white Teflon lined steel autoclave as well as in a hydrothermal bomb. In an autoclave attempt: The autoclave was sealed and maintained at 130 °C for 9 h. In a hydrothermal bomb attempt: the reaction took place in a 150 mL white Teflon liner which was placed into the hydrothermal bomb and heated in an oven at 130 °C for 9 h. In both reactions, the reaction was cooled down naturally to room temperature. The products were collected by centrifugation and washed with water and ethanol several times, before dried at 40 °C in an oven. The samples synthesized in the autoclave and hydrothermal bomb were named A2 and A3, respectively.

Characterization

The crystal structures of A2 and A3 were studied by X-ray diffraction (XRD) using a Bruker D8 Advance X-ray diffractometer. Diffractograms were measured using a Cu-Kα radiation source (1.5418 Å) in the range of 10.0–80.0°. Molecular analysis of the samples was performed by Fourier transform Infrared (FT-IR) spectroscopy using IR Thermo Scientific Smart iTR spectrophotometer. The spectrophotometer recorded in the wavenumber range of 4000–400 cm^{-1}. UV–Vis diffuse reflectance spectroscopy (DRS) was used to study the optical properties of A2 and A3, using an Agilent Cary UV–Vis spectrophotometer. The spectra were recorded in the range of 400–800 nm.

Calculations

Results computed and presented in this work were based on spin polarized DFT-based calculations performed with the Vienna Ab-initio Simulation Package [22]. The interactions between core and valence electrons were represented using the projector augmented wave (PAW) method [23]. The general gradient approximation (GGA) [24] exchange-correlation (XC) functional with the Perdew–Burke–Ernzerhof (PBE) parametrization was employed for DFT+U within the formalism of Dudarev et al. [25], with an $U_{\text{eff}} = 8$ eV identified in an earlier study [26]. For the hybrid-DFT calculations, the HSE06 XC functional was used [27–29], with a screening parameter of 0.2 Å^{-1}. Long distance dispersion corrections were included using the D3 approach of Grimme et al. [30]. The plane wave expansion cutoff was set to 500 eV and the force convergence criterion to cell relaxation was 0.01 eV/Å. Monkhorst-Pack [31] meshes ($5 \times 5 \times 5$ for the primitive unit cell, $5 \times 5 \times 3$ for conventional unit cell, and single Γ point for the $2 \times 2 \times 2$ supercell) were employed to sample the Brillouin zone in reciprocal space. Band structure calculations were performed at the optimized structure along high-symmetry directions obtained from the Bilbao Crystallographic Server [32–34] and plotted using the Wannier90 code [35, 36]. The phase stability diagram of Cu_4O_3 for a range of accessible chemical potentials was computed using the CPLAP (Chemical Potential Limits Analysis Program) [37], taking into account its limiting competing phases. The extent of defect charge distribution was studied using the Bader scheme as implemented in the Henkelman code [38–40]. Graphical drawings were produced using VESTA [41]. Excitonic and spin–orbit coupling effects were not taken into account.

B3LYP calculations were first performed using the all-electron CRYSTAL17 code [42, 43], in conjunction with triple-ζ-valence + polarization Gaussian-type basis sets optimized for copper oxides by Linnera et al. [44, 45]. In CRYSTAL, the convergence of the real-space summation of the Coulomb and exchange contributions to the Hamiltonian matrix is controlled by five overlap criteria. The values used in this study were 10^{-7}, 10^{-7}, 10^{-7}, 10^{-7}, and 10^{-14}. A Monkhorst-Pack shrinking factor of 8 was used to sample the first Brillouin zone and a denser Gilat net consisting of 16 points was used in the evaluation of the Fermi energy and density matrix [42]. The tuning of the exact exchange fraction used in B3LYP was done according to the self-consistent scheme proposed by Skone et al. [46] and implemented by Erba et al. [47]. Following that procedure, the system-specific exact exchange fraction, defined as inversely proportional to the static electronic dielectric constant ϵ_∞, is calculated iteratively until it changes by less than 0.1 % between two subsequent iterations. CRYSTAL17 uses a fully-automated, computationally-efficient implementation of the self-consistent (global) hybrid functional, where the dielectric functional is computed adopting a Coupled-Perturbed-Hartree-Fock/Kohn-Sham (CPHF/KS) approach [42]. A value of 0.17407 (17.407 % of exact exchange) used within B3LYP was obtained and demonstrated to yield accurate results for Cu_4O_3 [48].

Similarly to CuO, the conventional and primitive unit cells of Cu_4O_3 (illustrated in Figure 1) exhibit different geometries. In order to transform from the primitive to the conventional modelling cell, the following transformations were applied:

$$\begin{gathered} P \rightarrow C \\ \begin{pmatrix} -\frac{1}{2} & \frac{1}{2} & \frac{1}{2} \\ \frac{1}{2} & -\frac{1}{2} & \frac{1}{2} \\ \frac{1}{2} & \frac{1}{2} & -\frac{1}{2} \end{pmatrix} \end{gathered} \tag{1}$$

where P and C stand for primitive and conventional, respectively. The simulation cell, in both the primitive and conventional crystallographic cell case was carefully tested and set up in such a way to reproduce the appropriate magnetic propagation vector discussed earlier. The equivalence between the two modelling cells was confirmed and the primitive one chosen for the subsequent defects study, in order to reduce the computational cost when compared to the conventional cell.

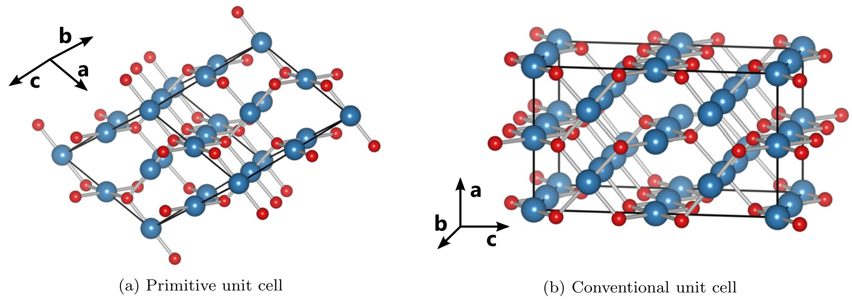

Fig. 1: Schematic representation of different ways to define the modelling unit cell of Cu_4O_3. Blue and red sphere represent copper and oxygen atoms, respectively.

Modelling of defects

Studied native defects in Cu_4O_3 include simple vacancies (V_{Cu} and V_O), antisites (Cu_O and O_{Cu}), and interstitials in three different positions within the simulation cell (Cu_{i-n} and O_{i-n}, with $n = 1, 2, 3$, identified using the PyCDT package [49] and shown in Figure 2). Each defect is modelled in a $2 \times 2 \times 2$ supercell, obtained by expanding the primitive unit cell, with a corresponding defect concentration of 1.56 and 2.08 % for impurities occurring on the Cu site and O site, respectively (as a result of the unequal number of Cu and O atoms in the unit cell).

The formation energy of a defect X in charge state q is defined as [50, 51]:

$$E^f[X^q] = E_{\text{tot}}[X^q] - E_{\text{tot}}[\text{bulk}] - \sum_i n_i \mu_i + q(E_F + \epsilon^{\text{H}}_{\text{VBM}}) + E_{\text{corr}}. \tag{2}$$

$E_{\text{tot}}[X]$ is the total energy derived from a supercell calculation containing the defect X, and $E_{\text{tot}}[\text{bulk}]$ is the total energy for the perfect crystal using an equivalent supercell. The integer n_i indicates the number of atoms of type i (host atoms or impurity atoms) that have been added to ($n_i > 0$) or removed from ($n_i < 0$) the supercell to form the defect, and μ_i are the corresponding chemical potentials of the considered species (related through $\Delta\mu_i = \mu_i - \mu_i^\circ$, where μ_i° is the chemical potential of the element i in its standard phase). The chemical potentials represent the energy of the reservoirs with which atoms are being exchanged. E_F represents the electron chemical potential, which ranges from the valence to the conduction band edges, $\epsilon^{\text{H}}_{\text{VBM}}$ is the eigenvalue of the valence band maximum of the pristine bulk material. Finally, E_{corr} is a correction term that accounts for finite-size effects in the calculations of charged defects as well as alignment of the band edges between the bulk and the defective supercells, performed using the SXDEFECTALIGN code by Freysoldt et al. [52]. The thermodynamic transition levels (ionization levels) of a given defect, $\varepsilon(q_1/q_2)$, correspond to the Fermi-level position at which a given defect changes from one charge state (q_1) to another (q_2):

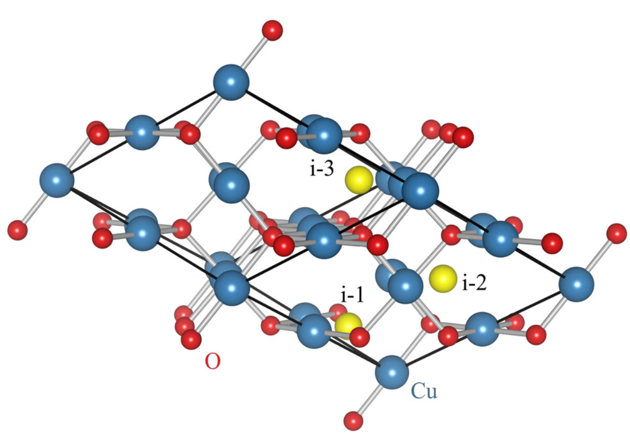

Fig. 2: Schematic representation of identified suitable interstitial position within the primitive crystal lattice of Cu_4O_3. Interstitial positions are labelled with black letters from i–1 to i–3.

$$\epsilon(q_1/q_2) = \frac{E^f[X^{q_1}] - E^f[X^{q_2}]}{q_2 - q_1}. \tag{3}$$

The allowed values of $\Delta\mu_i$ are determined from a set of thermodynamic limits. The upper limit is given by $\Delta\mu_i \leq 0$ where element i precipitates to its standard state, *e.g.*, O_2(g) (referred to half of the total energy of an oxygen molecule) and Cu(s). Furthermore, to avoid the formation of secondary solid phases, the chemical potentials must also be bound by:

$$2\Delta\mu_{Cu} + \Delta\mu_O \leq \Delta H_f(Cu_2O), \tag{4}$$

$$\Delta\mu_{Cu} + \Delta\mu_O \leq \Delta H_f(CuO) \tag{5}$$

with ΔH_f being the standard enthalpy of formation at zero K. The total energies of the phases competing with Cu_4O_3, *i.e.*, Cu_2O and CuO, were calculated using their respective unit cells. Cu_2O was modelled in a simple cubic non-magnetic cell, while for monoclinic CuO, a magnetic simulation cell containing 16 atoms was used together with the antiferromagnetic spin ordering leading to the observed lowest energy configuration [53, 54].

Results and discussion

Structural properties and optical measurements

The crystal structure and phase purity of the products were characterized by XRD. The XRD patterns of A2 and A3 are shown in Figure 3. All diffraction peaks of A2 are indexed to tetragonal Cu_4O_3 (COD-9000603), which is consistent with previously reported pure Cu_4O_3 [5, 9, 12]. The diffraction peaks of A3 are in good agreement with COD-2106291. The XRD patterns of both products were found to exhibit Cu_4O_3 nature. However, the XRD pattern of the A3 sample shows, together with the already identified Cu_4O_3 an additional peak at $2\theta = 12.76°$ which corresponds to an intermediate phase $Cu_2(OH)_3NO_3$ (COD-9008310). The existence of intermediate precursor phase $Cu_2(OH)_3NO_3$ registered in the XRD pattern of the prepared A3 sample is due to the incomplete decomposition of the starting material $Cu(NO_3)_2\,3H_2O$ [5, 55]. The diffraction peaks of A2 and A3 are sharp and strong in intensity, without any other obvious impurity peaks, indicating high crystallinity and purity.

The average crystallite size (D) for the samples was obtained from main peaks and was calculated using the Debye-Scherrer formula:

$$D = \frac{k\lambda}{\beta \cos\theta}, \tag{6}$$

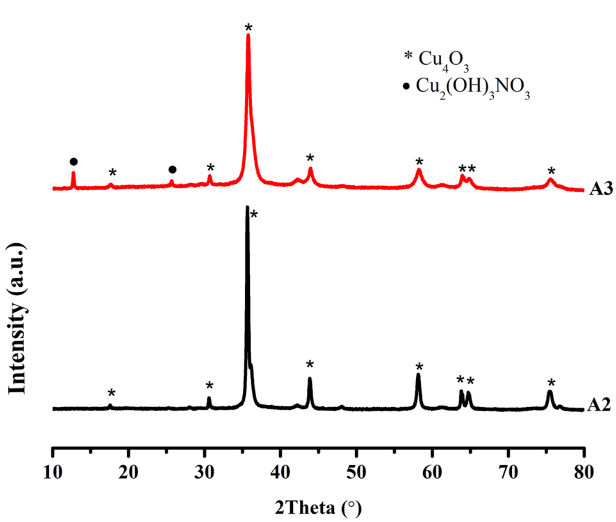

Fig. 3: XRD patterns of Cu_4O_3 (A2 sample) and Cu_4O_3 with traces of $Cu_2(OH)_3NO_3$ (A3 sample).

where D is the crystallite size, k the shape factor, λ the wavelength of the X-ray beam, θ the diffraction angle, and β the full width at half maximum (FWHM) of the peak in the XRD pattern. The calculated crystallite size of the A2 and A3 samples was found to be 27.7 and 6.9 nm, respectively, indicating that the synthesized powders are made up of nano-particles.

Figure 4 shows the FT-IR spectra of Cu_4O_3 and Cu_4O_3 with $Cu_2(OH)_3NO_3$ nanopowders. The bands below 1000 cm^{-1} can be observed in both spectra, which are assigned to the Cu–O vibration modes of Cu_4O_3 [9, 16, 19, 56]. The bands observed at 1049, 1051, 2176, and 2177 cm^{-1} are related to C–H bending and stretching [9, 56]. The band at 1337 cm^{-1} was ascribed to O–H vibrations of adsorbed water (moisture) and hydroxyls in the structure of the A3 sample [9], while the band at 1419 cm^{-1} in the A3 spectrum may be due to the stretching vibrations of NO_3^- [57].

UV–Vis diffuse reflectance spectroscopy was used to investigate the optical properties of the samples (Figure 5a). The Tauc plots obtained from the UV–Vis diffuse reflectance measurements are shown in Figure 5b. By plotting $(h\nu F(R))^2$ as a function of energy, a line of best fit through the point of maximum gradient within each Tauc plot, the direct optical band gaps were determined to be 1.54 and 1.49 eV for Cu_4O_3 and Cu_4O_3 + $Cu_2(OH)_3NO_3$, respectively. The band gap of A2 is within the range of the band gap of the previously synthesized Cu_4O_3 [7, 19, 20, 58]. From the Tauc plots, none of the data sets appear to produce a typical plot as there are multiple absorption steps in each case. Such Tauc plots confirm the presence of mixed valence copper ions present in the A2 sample, while in the case of the A3 sample they are the consequence of the compound mixture. However, the most notable step was fitted to obtain the band gaps.

Electronic properties

As demonstrated in previous works concerning the modelling of bulk Cu_4O_3 [17, 26], local and semi-local DFT was found unsatisfactory for the description of its electronic properties. Hybrid-DFT, in the form of HSE06, captures the correct nature of the first band–to–band transition as indirect, but produces a difference between the indirect and direct band gap which underestimates experimental values. By tuning the exact exchange within HSE06, the electronic structure is influenced only by lowering the position of the conduction band relative to the valence band, hence decreasing the band gap value without significantly altering its structure (as outlined in an earlier work [48]). However, since there are many other available approximations for the XC functional, the question arises whether another functional can accurately reproduce the electronic properties

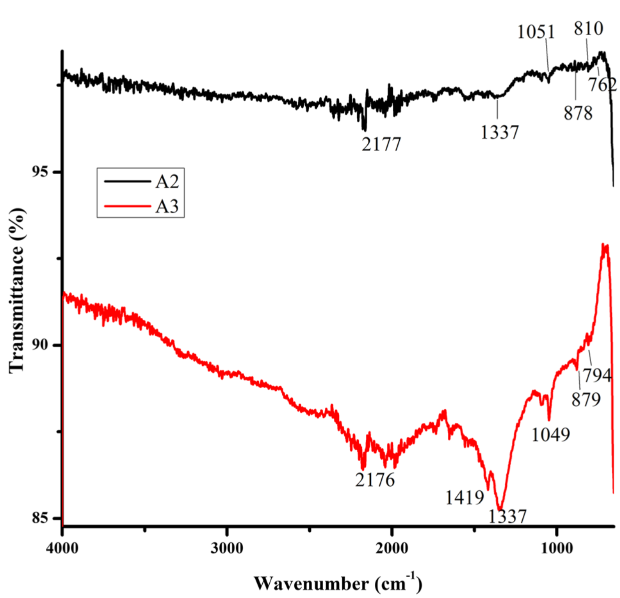

Fig. 4: FT-IR spectra of Cu_4O_3 (A2 sample) and Cu_4O_3 with traces of $Cu_2(OH)_3NO_3$ (A3 sample).

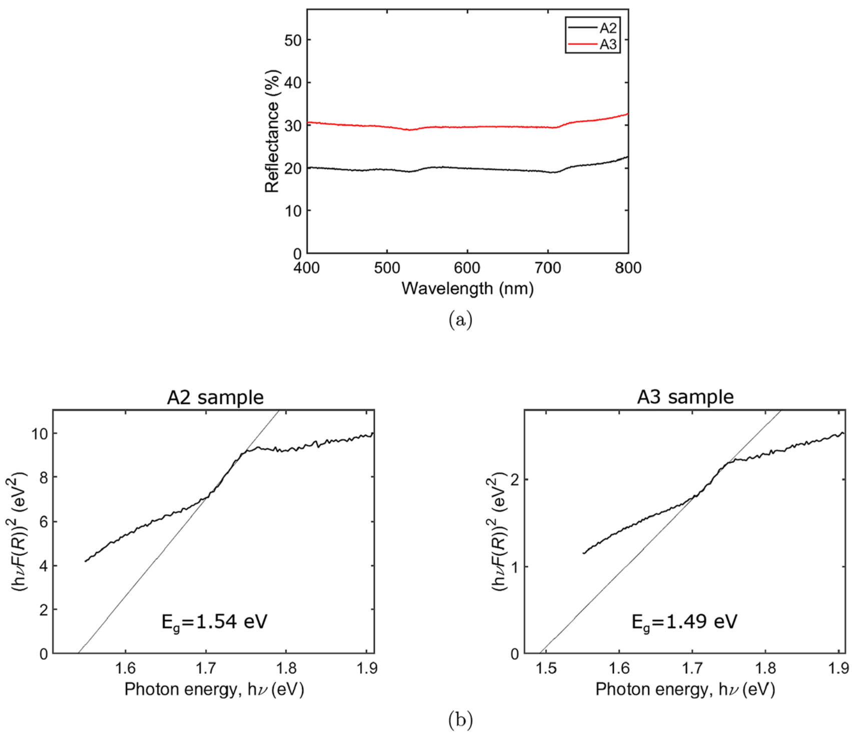

Fig. 5: Diffuse reflectance spectra of the A2 and A3 samples in (a), together with the corresponding Tauc plots in (b).

of Cu_4O_3 or whether this material cannot be modelled accurately by DFT? Unlike HSE06, B3LYP is a global functional, where the amount of HF exchange included does not depend on the distance between electrons. In order to test the accuracy of a different type of hybrid functional, B3LYP was used to calculate the electronic properties of Cu_4O_3. The calculated electronic structure using the self-consistently determined optimal fraction for B3LYP (SC-B3LYP) is shown in Figure 6. The obtained SC-B3LYP indirect and direct band gaps read 1.89 and 2.41 eV for the ground state antiferromagnetic ordering. This value is somewhat higher than the experimentally noted gap for the pure A2 sample. However, for a ferromagnetic ground state of Cu_4O_3, a direct band gap of 1.44 eV is found, indicating that the temperature-induced rearrangement of the spin order may influence the electronic structure significantly, similar to what is observed in CuO [53].

Phase stability

Calculated formation enthalpies of Cu_4O_3 are reported in Table 3. Both HSE06 (with standard 20 % exact exchange) and SC-B3LYP show similar trends with results being reasonably close to experimental values. The slight overestimation of SC-B3LYP values is not necessarily a surprise, since it is known that the B3LYP functional does not provide accurate total energies for metallic Cu, as demonstrated in earlier works [61]. Limits for the chemical potential range valid for pristine Cu_4O_3 were calculated from available formation enthalpies and constraints set by the evolution of competing phases, in this case Cu_2O and CuO.

In order to bypass stability issues originating from the use of different functionals, values for formation enthalpies entering the stability range calculation were taken from available experimental data. The calculated phase stability region for Cu_4O_3 is shown in Figure 7. The thermodynamic stability window of Cu_4O_3 is narrow, in accord with the observed difficulty of synthesizing pure samples without Cu_2O or CuO being present. Effectively, Cu_4O_3 can only be created under Cu-rich/O-poor conditions, with chemical potential values reading $\Delta\mu_{Cu} = -0.157$ and $\Delta\mu_O = -1.437$ eV. Furthermore, the observed narrowness of the available stability region for Cu_4O_3 indicates that the choice of functional would not substantially alter the defect formation energies, calculated at this specific point in chemical potential space.

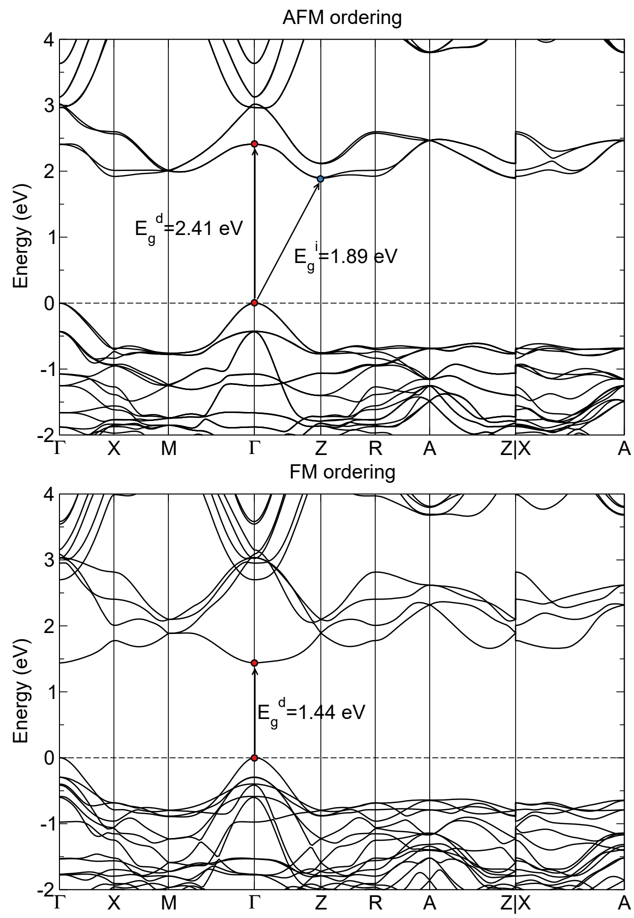

Fig. 6: Computed electronic band structure of Cu_4O_3 for two different magnetic orderings using SC-B3LYP, where the fraction of exact exchange was obtained in a self-consistent manner. The dashed line indicates the highest occupied valence state.

Table 3: Calculated enthalpies of formation (eV/formula unit) for Cu_4O_3. Values for Cu_2O and CuO are shown for validation of values within a used functional.

	ΔH_f (Cu_2O)	ΔH_f (Cu_4O_3)	ΔH_f CuO
HSE06	−1.66	−4.92	−1.57
SC-B3LYP	−2.21	−5.32	−1.69
Experiment	−1.75 [59]	−4.69 (at 427 °C) [60]	−1.59 [59]
		−4.88 (at 25 °C) [60]	
		−5.94 ± 25 (at 25 °C) [60]	

As outlined previously, Cu_4O_3 contains two distinct Cu and O atoms. They can be distinguished through their coordination number or oxidation (valence) state. The first one (Cu^{1+}) is a cuprous Cu binding two nearest neighbouring O atoms (labelled O–1) in a linear arrangement, while the other (Cu^{2+}) is a cupric Cu surrounded by four O atoms in an almost square planar configuration. Each O atom, on the other hand, binds four Cu atoms, with the difference that the first (O–1) binds four Cu^{2+} atoms while the second (O–2) binds two Cu^{1+} and two Cu^{2+} atoms. The Bader charge analysis provides a useful way of determining those differences in order to detect distinct impurity sites within the cell. Results for clean Cu_4O_3 are presented in Table 4. Despite the nominal charge state of −2, the two O atoms show small differences in accumulated charge of $\Delta = 0.02e^-$, regardless of the chosen functional approximation. Interestingly, DFT+U results follow the same trend as HSE06 and SC-B3LYP ones, with absolute values being considerably reduced. However, results presented in the following paragraphs consider mostly SC-B3LYP results, owing to the accurate description of the initial

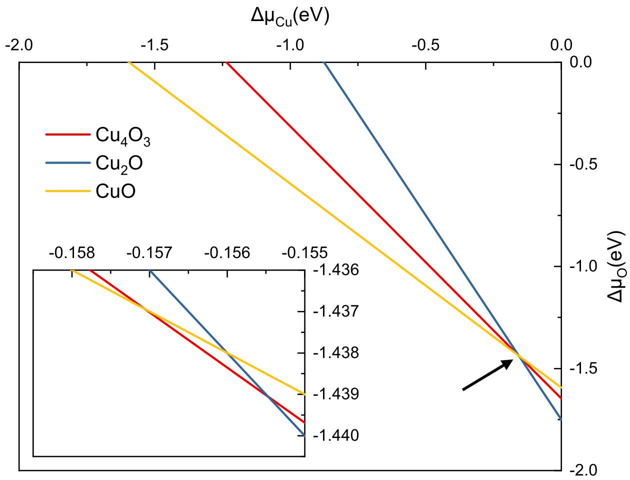

Fig. 7: Phase stability in the range of accessible chemical potentials for Cu_4O_3, constructed from available experimental data. Limits are imposed by the formation of competing phases, *i.e.*, Cu_2O and CuO. The black arrow denotes the narrow stability region of Cu_4O_3, emphasized further in the zoom-in plot.

electronic structure. Comparison with DFT+U or HSE06 results is drawn where appropriate. Following the outlined analysis, it is noted that vacancy and antisite defects modelled in Cu_4O_3 include two distinct configurations in order to capture all possible sites.

Intrinsic defects

The calculated formation energies of simple neutral defects in Cu_4O_3 are presented in Figure 8, with vacancies shown on the left hand side. The two Cu vacancies, corresponding to the removal of one Cu^{1+} or Cu^{2+} atom are labelled as $V_{Cu^{1+}}$ and $V_{Cu^{2+}}$, respectively, while the two O vacancies are named V_{O-1} and V_{O-2} distinguishing between the sites identified earlier. Note how the calculated defect formation energies do not depend greatly on the functional approximation, retaining overall trends. This points towards the applicability of DFT+U calculations as an affordable approach for pre-screening of defects, while finer formation energy distributions should be obtained using a hybrid functional.

Removing a Cu^{1+} atom from the crystal lattice results in two dangling bonds from the neighbouring O atoms with mostly p character. The formation of a neutral $V_{Cu^{1+}}$ defect causes the two closest O atoms to relax away from the site, yet the overall influence on the lattice parameters is less than 0.8 % expansion. A neutral $V_{Cu^{1+}}$ defect creates a singly-unoccupied state in the otherwise empty electronic band structure (see Figure 9). The unoccupied acceptor level is located around 0.66 eV above the VB maximum in the spin majority channel, originating mainly from Cu d and O p states. The created hole is highly delocalized in real space (not shown explicitly). As the defect becomes occupied in the −1 charge state, no further relaxation effects are noted and the excess charge is readily incorporated into the lattice. $V_{Cu^{1+}}$ is a shallow acceptor in Cu_4O_3 (see Figure 10), existing as a charged defect across the whole range of available Fermi levels, with the $\epsilon(0/-1)$ transition level located inside the valence band maximum (VBM).

The cost to create a neutral $V_{Cu^{2+}}$ is much higher than that of a neutral $V_{Cu^{1+}}$, which is anticipated as it essentially describes the energy required to break the four Cu^{2+}–O bonds (compared to two Cu^{1+}–O ones). The removal of a Cu^{2+} atom leads to a relaxation of the nearest O atoms away from the defect site, similar to the $V_{Cu^{1+}}$

Table 4: Bader charge analysis of Cu_4O_3 using three different approximations for the XC functional. Values reported in e^-.

	Cu^{1+}	Cu^{2+}	O–1	O–2
DFT+U	+0.534	+0.913	−0.959	−0.936
HSE06	+0.563	+1.122	−1.130	−1.112
SC-B3LYP	+0.545	+1.070	−1.089	−1.065

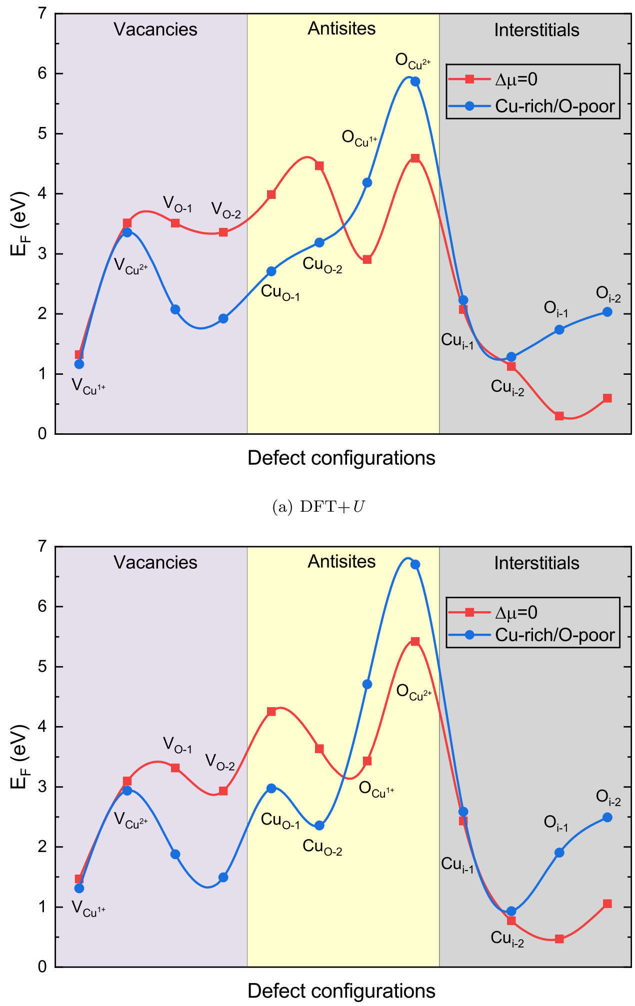

(a) DFT+U

(b) SC-B3LYP

Fig. 8: Formation energy of all native defects occurring in Cu_4O_3 in the charge neutral state. Results are presented for two different approximation for the XC functional as well as two distinct chemical potential limits. The red line illustrates the maximally Cu- and O-rich conditions ($\Delta\mu_i = 0$), while the blue line represents the only stability point of Cu_4O_3 discussed earlier. The actual values are represented with filled symbols, while the lines are visual guidelines.

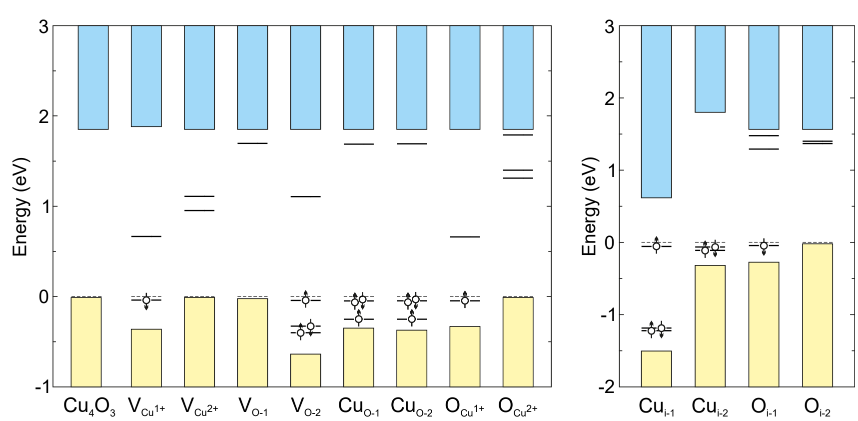

Fig. 9: Schematic representation of the electronic densities of states of clean and defective Cu_4O_3 in their respective charge neutral state. The dashed line indicates the highest occupied band and up/down arrows represent different spin channels.

defect. The neighbouring O atoms relax towards each other, alternating the O–O distance for 0.02–0.05 Å, in order to maximize their bond overlap. When the $V_{Cu^{2+}}$ defect becomes populated, the ions relax slightly further away from the defect site due to increased Coulomb repulsion. The $\epsilon(0/-1)$ ionization level is found inside VBM, whereas the $\epsilon(-1/-2)$ transition acts as a deep acceptor located 0.47 eV above the VBM.

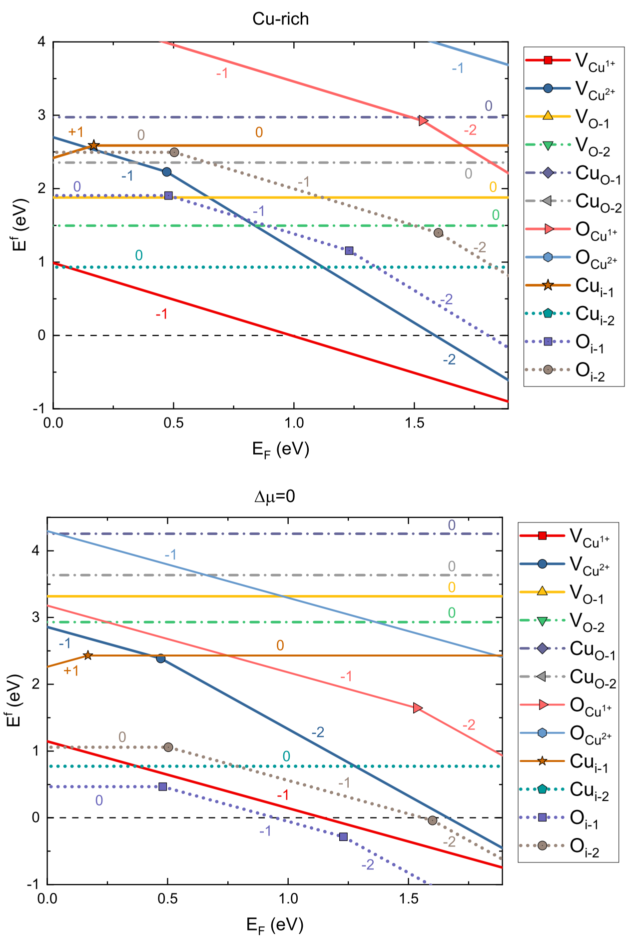

Fig. 10: Formation energy of native charged defects occurring in Cu_4O_3, plotted as a function of the Fermi level varying from the top of the valence band maximum to the bottom of the conduction band minimum, under conditions chosen in Figure 9. The slope of the lines denotes the charge state and the solid dots represent the transition levels ε.

Removing one O–1 or O–2 atom leaves the two electrons from the surrounding Cu atoms weakly bound to their respective hosts. The doubly unoccupied defect states are localized well below the conduction band minimum (CBM), resulting in a lattice relaxation in order to accommodate the defect. Both V_{O-1} and V_{O-2} are stable as neutral defects, with the corresponding ionization levels well inside the valence band, indicating that they do not act as charge compensating defects in Cu_4O_3.

Antisite defects in Cu_4O_3 are unlikely to form due to their high formation energies. Moreover, Cu_{O-1} and Cu_{O-2} exist as neutral defects over the entire Fermi level range and, similar to O vacancies do not participate in charge compensating phenomena. $O_{Cu^{1+}}$ and $O_{Cu^{2+}}$ are stable in the −1 charged state with the $OO_{Cu^{1+}}$ possessing a deep $\varepsilon(-1/-2)$ transition level at 1.53 eV above the VBM, while the same $\varepsilon(-1/-2)$ for $OO_{Cu^{2+}}$ is located inside the CBM.

Out of the three suitable positions for interstitial atoms (shown earlier in Figure 2), i–2 and i–3 relax to yield identical behaviour due to symmetry of the lattice site where the defect is incorporated. Cu_{i-1} is found to incorporate into the plane of zig-zag Cu^{1+} atoms, causing the neighbouring Cu atom to relax away from the similarly charged interstitial site. Cu_{i-1} behaves as a relatively shallow donor, with a $\varepsilon(+1/0)$ ionization level at approximately 0.17 eV above the VBM. However, the formation energy of the Cu_{i-1} defect lies relatively high around 2.5 eV, compared to other defects available in Cu_4O_3. On the other hand, the formation energy of neutral Cu_{i-2} is approximately 1 eV, where a simple lattice rearrangement allows the interstitial to fully bind onto its neighbouring O atoms. Cu_{i-2} is found in the neutral charge state across the whole Fermi level range, with the $\varepsilon(+1/0)$ thermodynamic transition located well in the VBM.

Interstitial O incorporated in position 1, O_{i-1}, binds actively to nearest neighbouring Cu atoms, inducing a charge transfer process, with a Bader charge value of $-0.96\ e^-$ being very close to $-1.08\ e^-$ found on a O atom located far away from the defect site. O_{i-1} acts as a deep acceptor in Cu_4O_3, with the transition levels $\varepsilon(0/-1)$ and $\varepsilon(-1/-2)$ located 0.48 and 1.23 eV above the VBM. O_{i-2} is found to behave in a similar manner to O_{i-1}, with the $\varepsilon(0/-1)$ and $\varepsilon(-1/-2)$ ionization levels 0.50 and 1.60 eV above the VBM, respectively.

Trends in formation energies

Altogether, there is a complex interplay between the formation of defects and conditions under which they are formed in Cu_4O_3. From the obtained plot of the formation energy as a function of the Fermi-level position for all intrinsic defects, $V_{Cu^{1+}}$ is the lowest energy acceptor defect for Cu_4O_3 created under Cu-rich conditions. It should also be noted that the formation energy of neutral Cu_{i-2} is 0.05 eV lower than that of negatively charged $V_{Cu^{1+}}$, although for a very small range of Fermi levels around the VBM. However, the ionization levels of Cu_{i-2} are deep in the valence band, indicating that Cu_{i-2} will not act as an effective hole compensating defect. Hence, Cu_4O_3 grown under the narrow span of available conditions will be a *p*-type semiconductor in nature. Moreover, there are almost no intrinsic *n*-type defects present to play a large role in the conductivity of Cu_4O_3. Finally, the formation energies of neither oxygen vacancies nor oxygen interstitials are found low enough to drive the conversion of Cu_4O_3 towards Cu_2O or CuO, respectively, as discussed when analysing the stoichiometry of paramelaconite earlier in the introduction.

The power of the computational approaches to materials modelling is that one can modify individual parameters and observe their effect on certain properties. In this case, the growth conditions were altered through the corresponding chemical potential to study the behaviour of Cu_4O_3 under rather unphysical conditions which favour the formation of CuO or Cu_2O. The calculated formation energies under equal chemical potential limits (Cu-rich/O-rich, where $\Delta\mu_i = 0$) is shown in Figure 10. In this case the O_{i-1} becomes the dominant defect in Cu_4O_3, with a neutral formation energy of only 0.5 eV, which is low enough to cause structural instability (oxidation) towards the formation of CuO. Furthermore, O_{i-1} has two acceptor transitions deep inside the band gap, worsening drastically the *p*-type conductivity compared to Cu_4O_3 formed under Cu-rich conditions.

Conclusion

The ground state properties and native point defects of Cu_4O_3 were modelled using density functional theory calculations. The stability region of Cu_4O_3 was assessed, depending on the varying chemical potentials of constituting species. Based on the analysis outlined, several significant findings were identified:

- Global range hybrid functionals outperform their range-separated analogues in the case of Cu_4O_3, where results close to experimental ones were obtained using B3LYP-based calculations with a self-consistently determined amount of exact exchange within.
- Cu_4O_3 is found to be thermodynamically stable in a very narrow range of accessible chemical potentials. This corroborates the experimentally noted sensitivity upon synthesis conditions.
- Under the observed growth conditions (Cu-rich), Cu_4O_3 demonstrates good intrinsic *p*-type conductivity arising from vacancy defects readily occurring on the Cu^{1+} atomic site.
- Intrinsic defects are not a source of *n*-type conductivity in Cu_4O_3 because they are unable to act as shallow donors or to compensate *p*-type conductivity.

However, whilst interpreting results outlined in this work, several limitations apply. Thermodynamic stability conditions as well as defect related properties (formation energies, migration barriers, etc.) depend on temperature effects, whose extent is inaccessible within the given theoretical framework. Despite those obvious constraints, the results obtained provide insights into difficulties related to obtaining pure Cu_4O_3 and maintaining it stable over longer periods of time, further exemplified by the experimental difficulties in synthesising phase-pure Cu_4O_3 samples.

Acknowledgments: We acknowledge the Cardiff University School of Chemistry for a PhD studentship for AŽ and the Royal Society DfID Africa programme for funding. NYD acknowledges the UK Engineering and Physical Sciences Research Council (EPSRC) for funding (Grant No. EP/S001395/1). This work was performed using the computational facilities of the Advanced Research Computing @ Cardiff (ARCCA) Division, Cardiff University. Via our membership of the UK's HPC Materials Chemistry Consortium, which is funded by EPSRC (EP/L000202), this work made use of the ARCHER facility, the UK's national high-performance computing service, which is funded by the Office of Science and Technology through EPSRC's High End Computing Programme.
Research funding: This work was funded by Cardiff University, Royal Society, and Engineering and Physical Sciences Research Council (EP/S001395/1, EP/L000202).

References

[1] C. Frondel. *Am. Mineral.* **26**, 657 (1941).
[2] N. Datta, J. W. Jeffery. *Acta Crystallogr. B* **34**, 22 (1978).
[3] M. O'Keeffe, J.-O. Bovin. *Am. Mineral.* **63**, 180 (1978).
[4] P. E. Morgan, D. E. Partin, B. L. Chamberland, M. O'Keeffe. *J. Solid State Chem.* **121**, 33 (1996).
[5] L. Zhao, H. Chen, Y. Wang, H. Che, P. Gunawan, Z. Zhong, H. Li, F. Su. *Chem. Mater.* **24**, 1136 (2012).
[6] N. J. Long, A. K. Petford-Long. *Ultramicroscopy* **20**, 151 (1986).
[7] J. F. Pierson, A. Thobor-Keck, A. Billard. *Appl. Surf. Sci.* **210**, 359 (2003).
[8] D. S. Murali, S. Aryasomayajula. *Appl. Phys. A* **124**, 279 (2018).
[9] W. Wang, L. Zhu, P. Lv, G. Liu, Y. Yu, J. Li. *ACS Appl. Mater. Interfaces* **10**, 37287 (2018).
[10] N. Martić, C. Reller, C. Macauley, M. Löffler, B. Schmid, D. Reinisch, E. Volkova, A. Maltenberger, A. Rucki, K. J. J. Mayrhofer, G. Schmid. *Adv. Energy Mater.* **9**, 1901228 (2019).
[11] M. A. M. Patwary, C. Y. Ho, K. Saito, Q. Guo, K. M. Yu, W. Walukiewicz, T. Tanaka. *J. Appl. Phys.* **127** (2020), https://doi.org/10.1063/1.5144205.
[12] H. S. Kim, P. Yadav, M. Patel, J. Kim, K. Pandey, D. Lim, C. Jeong. *Superlattice. Microst.* **112**, 262 (2017).
[13] L. Pinsard-Gaudart, J. Rodríguez-Carvajal, A. Gukasov, P. Monod. *Phys. Rev. B* **69**, 104408 (2004).
[14] D. Djurek, M. Prester, D. Drobac, M. Ivanda, D. Vojta. *J. Magn. Magn Mater.* **373**, 183 (2015).
[15] E. M. Tejada-Rosales, J. Rodríguez-Carvajal, N. Casañ-Pastor, P. Alemany, E. Ruiz, M. S. El-Fallah, S. Alvarez, P. Gómez-Romero. *Inorg. Chem.* **41**, 6604 (2002).
[16] L. Debbichi, M. C. Marco de Lucas, J. F. Pierson, P. Kruger. *J. Phys. Chem. C* **116**, 10232 (2012).
[17] M. Heinemann, B. Eifert, C. Heiliger. *Phys. Rev. B* **87**, 115111 (2013).
[18] L. Debbichi, M. C. Marco de Lucas, P. Krüger. *Mater. Chem. Phys.* **148**, 293 (2014).
[19] D. S. Murali, A. Subrahmanyam. *J. Phys. Appl. Phys.* **49**, 375102 (2016).
[20] D. Reppin, A. Polity, B. Meyer, S. Shokovets. *Mater. Res. Soc. Symp. Proc.* **1494**, 25 (2012).
[21] Y. Wang, S. Lany, J. Ghanbaja, Y. Fagot-Revurat, Y. P. Chen, F. Soldera, D. Horwat, F. Mücklich, J. F. Pierson. *Phys. Rev. B* **94**, 245418 (2016).
[22] G. Kresse, D. Joubert. *Phys. Rev. B* **59**, 1758 (1999).
[23] P. E. Blöchl. *Phys. Rev. B* **50**, 17953 (1994).
[24] J. P. Perdew, K. Burke, M. Ernzerhof. *Phys. Rev. Lett.* **77**, 3865 (1996).
[25] S. L. Dudarev, G. A. Botton, S. Y. Savrasov, C. J. Humphreys, A. P. Sutton. *Phys. Rev. B* **57**, 1505 (1998).
[26] A. Živković, A. Roldan, N. H. de Leeuw. *Phys. Rev. B* **99**, 035154 (2019).
[27] J. Heyd, G. E. Scuseria, M. Ernzerhof. *J. Chem. Phys.* **118**, 8207 (2003).
[28] J. Heyd, G. E. Scuseria. *J. Chem. Phys.* **121**, 1187 (2004).
[29] J. Heyd, G. E. Scuseria, M. Ernzerhof. *J. Chem. Phys.* **124**, 219906 (2006).
[30] S. Grimme, J. Antony, S. Ehrlich, H. Krieg. *J. Chem. Phys.* **132**, 154104 (2010).
[31] H. J. Monkhorst, J. D. Pack. *Phys. Rev. B* **13**, 5188 (1976).
[32] M. I. Aroyo, J. M. Perez-Mato, C. Capillas, E. Kroumova, S. Ivantchev, G. Madariaga, A. Kirov, H. Wondratschek. *Z. für Kristallogr. – Cryst. Mater.* **221**, 15 (2006).
[33] M. I. Aroyo, A. Kirov, C. Capillas, J. M. Perez-Mato, H. Wondratschek. *Acta Crystallogr. A* **62**, 115 (2006).
[34] M. I. Aroyo, J. M. Perez-Mato, D. Orobengoa, E. Tasci, G. De La Flor, A. Kirov. *Bulg. Chem. Commun.* **43**, 183 (2011).
[35] G. Pizzi, D. Volja, B. Kozinsky, M. Fornari, N. Marzari. *Comput. Phys. Commun.* **185**, 422 (2014).
[36] G. Pizzi, V. Vitale, R. Arita, S. Blügel, F. Freimuth, G. Géranton, M. Gibertini, D. Gresch, C. Johnson, T. Koretsune, J. Ibañez-Azpiroz, H. Lee, J.-M. Lihm, D. Marchand, A. Marrazzo, Y. Mokrousov, J. I. Mustafa, Y. Nohara, Y. Nomura, L. Paulatto, S. Poncé,

T. Ponweiser, J. Qiao, F. Thöle, S. S. Tsirkin, M. Wierzbowska, N. Marzari, D. Vanderbilt, I. Souza, A. A. Mostofi, J. R. Yates. *J. Phys. Condens. Matter* **32**, 165902 (2020).
[37] J. Buckeridge, D. Scanlon, A. Walsh, C. Catlow. *Comput. Phys. Commun.* **185**, 330 (2014).
[38] M. Yu, D. R. Trinkle. *J. Chem. Phys.* **134**, 064111 (2011).
[39] W. Tang, E. Sanville, G. Henkelman. *J. Phys. Condens. Matter* **21**, 084204 (2009).
[40] E. Sanville, S. D. Kenny, R. Smith, G. Henkelman. *J. Comput. Chem.* **28**, 899 (2007).
[41] K. Momma, F. Izumi. *J. Appl. Crystallogr.* **44**, 1272 (2011).
[42] R. Dovesi, V. R. Saunders, C. Roetti, R. Orlando, C. M. Zicovich-Wilson, F. Pascale, B. Civalleri, K. Doll, N. M. Harrison, I. J. Bush, P. D'Arco, M. Llunell, M. Causà, Y. Noël, L. Maschio, A. Erba, M. Rerat, S. Casassa. in *CRYSTAL17 User's Manual*, University of Torino, Torino (2017).
[43] R. Dovesi, A. Erba, R. Orlando, C. M. Zicovich-Wilson, B. Civalleri, L. Maschio, M. Rérat, S. Casassa, J. Baima, S. Salustro, B. Kirtman. *WIREs Comput. Mol. Sci.* **8**, 1 (2018).
[44] J. Linnera, G. Sansone, L. Maschio, A. J. Karttunen. *J. Phys. Chem. C* **122**, 15180 (2018).
[45] J. Linnera, A. J. Karttunen. *Phys. Rev. B* **96**, 014304 (2017).
[46] J. H. Skone, M. Govoni, G. Galli. *Phys. Rev. B* **89**, 195112 (2014).
[47] A. Erba. *J. Phys. Condens. Matter* **29**, 314001 (2017).
[48] A. Živković, N. H. de Leeuw, B. G. Searle, L. Bernasconi. *J. Phys. Chem. C* **124**, 24995 (2020).
[49] D. Broberg, B. Medasani, N. E. Zimmermann, G. Yu, A. Canning, M. Haranczyk, M. Asta, G. Hautier. *Comput. Phys. Commun.* **226**, 165 (2018).
[50] C. G. Van De Walle, J. Neugebauer. *J. Appl. Phys.* **95**, 3851 (2004).
[51] S. B. Zhang, J. E. Northrup. *Phys. Rev. Lett.* **67**, 2339 (1991).
[52] C. Freysoldt, J. Neugebauer, C. G. Van de Walle. *Phys. Rev. Lett.* **102**, 016402 (2009).
[53] X. Rocquefelte, M.-H. Whangbo, A. Villesuzanne, S. Jobic, F. Tran, K. Schwarz, P. Blaha. *J. Phys. Condens. Matter* **22**, 045502 (2010).
[54] X. Rocquefelte, K. Schwarz, P. Blaha. *Sci. Rep.* **2**, 759 (2012).
[55] Z. Jiang, S. Tian, S. Lai, R. D. McAuliffe, S. P. Rogers, M. Shim, D. P. Shoemaker. *Chem. Mater.* **28**, 3080 (2016).
[56] J. Thanuja, Udayabhanu, G. Nagaraju, H. R. Naika. *SN Appl. Sci.* **1**, 1646 (2019).
[57] A. Srikhaow, S. M. Smith. *Appl. Catal. B Environ.* **130–131**, 84 (2013).
[58] J. Medina-Valtierra, C. Frausto-Reyes, G. Camarillo-Martínez, J. A. Ramírez-Ortiz. *Appl. Catal. Gen.* **356**, 36 (2009).
[59] D. R. Lide. *CRC Handbook of Chemistry and Physics, Internet Version 2005*, CRC Press, Boca Raton, FL (2005).
[60] K. J. Blobaum, D. Van Heerden, A. J. Wagner, D. H. Fairbrother, T. P. Weihs. *J. Mater. Res.* **18**, 1535 (2003).
[61] C. L. Bailey, L. Liborio, G. Mallia, S. Tomić, N. M. Harrison. *Phys. Rev. B* **81**, 205214 (2010).